**Proceedings of the ASME 2021 Fluids Engineering Division Summer Meeting**
**FEDSM2021**
**August 10 – August 12, 2021, Virtual Conference, Online**

# FEDSM2021-61832

# EFFECTS OF WING KINEMATICS ON MODULATING ODOR PLUME STRUCTURES IN THE ODOR TRACKING FLIGHT OF FRUIT FLIES

**Menglong Lei and Chengyu Li**

Department of Mechanical Engineering, Villanova University, Villanova, PA 19085

## ABSTRACT

Insects rely on their olfactory system to forage, prey, and mate. They can sense odorant plumes emitted from sources of their interests with their bilateral odorant antennae, and track down odor sources using their highly efficient flapping-wing mechanism. The odor-tracking process typically consists of two distinct behaviors: surging upwind and zigzagging crosswind. Despite the extensive numerical and experimental studies on the flying trajectories and wing flapping kinematics during odor tracking flight, we have limited understanding of how the flying trajectories and flapping wings modulate odor plume structures. In this study, a fully coupled three-way numerical solver is developed, which solves the 3D Navier-Stokes equations coupled with equations of motion for the passive flapping wings, and the odorant convection-diffusion equation. This numerical solver is applied to investigate the unsteady flow field and the odorant transport phenomena of a fruit fly model in both surging upwind and zigzagging crosswind cases. The unsteady flow generated by flapping wings perturbs the odor plume structure and significantly impacts the odor intensity at the olfactory receptors (i.e., antennae). During zigzagging crosswind flight, the differences in odor perception time and peak odor intensity at the receptors potentially help create stereo odorant mapping to track odor source. Our simulation results will provide new insights into the mechanism of how fruit flies perceive odor landscape and inspire the future design of odor-guided micro aerial vehicles (MAVs) for surveillance and detection missions.

## NOMENCLATURE

| | |
|---|---|
| $A_\phi$ | : Stroke angle amplitude |
| $b$ | : Wing spanwise length |
| $\bar{c}$ | : Mean wing chord length |
| $C$ | : Odor intensity |
| $C^*$ | : Non-dimensional odor intensity |
| $Ch$ | : Cauchy number |
| $C_L$ | : Lift coefficient |
| $f$ | : Flapping frequency |
| $G$ | : Torsional stiffness of the spring |
| $I$ | : Moment of inertia |
| $M_{aero}$ | : Moment due to the aerodynamic force |
| $M_{elastic}$ | : Moment due to the elastic force |
| $M_{gravity}$ | : Moment due to the gravitational force |
| $Re$ | : Reynolds number |
| $S$ | : Wing surface area |
| $u_i$ | : Velocity component |
| $U_i$ | : Face-centered velocity component |
| $\bar{U}_{tip}$ | : Averaged wing tip velocity |
| $\alpha$ | : Odor diffusivity |
| $\phi$ | : Wing stroke angle |
| $\theta$ | : Wing pitch angle |
| $\theta_0$ | : Rest angle |
| $\omega$ | : Angular velocity |
| $\rho_{air}$ | : Fluid density |
| $\nu$ | : Kinematic viscosity |

## INTRODUCTION

The behaviors of fruit flies while tracking odor source have been widely studied in the past few decades. They exhibit the ability to track odor source beyond visual field. Fruit flies require bilateral odorant input on the antennae to create a stereo-olfactory mapping to track odor source [1]. Li et al [2, 3] visualized the odor plume structure around fruit flies during forward flight using Lagrange particle tracing approach and confirmed that the antennae are well positioned to perceive the odor plume while avoiding wing-induced disturbance. This gives rise to a question: how is the odor landscape like near the antennae?

Experimental studies on the behaviors of fruit flies while tracking odor source have been conducted. Van Breugel et al [4] studied the odor tracking behaviors of fruit flies in a wind tunnel and described the two specific behaviors while encountering odor plume. Fruit flies zigzag crosswind to upwind when encountering and losing an odor plume. When they sense the odor plume again, they surge upwind to visual stimulus [5]. During odor tracking flight, fruit flies actively zigzag crosswind through the odor landscape to enhance odor filament detection of the two antennae and increase the sampling range. Meanwhile, the flapping motion of the two wings alters both the aerodynamics and odor landscape in the flow field which may increase the odor sensitivity and generate the odor intensity gradient to help locate the odor source. However, most previous studies on odor plume structures during odor-guided flight of insects are limited on experimental observation. Even though extensive experiments on flight trajectories during odor tracking flight were conducted, the lack of quantitative measurement method of odor intensity at small length scale makes it hard to understand the effects of flapping wings and flight trajectories on odor landscape. How the zigzagging crosswind motion and wing-induced flow generated by flapping wings impact the odor landscape near the antennae remains unknown.

In addition to experimental measurements, numerical simulation can be treated as an alternative approach to obtain the instantaneous odor landscape. One of the challenges to perform numerical simulation is to predict the wing kinematics during zigzagging crosswind motion. It has been proposed that the insect wings can achieve the fundamental aerodynamic functions passively. As insects apply their muscle force through wing leading-edge, they create a momentum that overcomes the aerodynamic loading, causing the wing to pitch without active control. Bergou et al [6] numerically investigated the required power for an insect to pitch its wing by solving the 2D Navier-Stokes equations and found that no additional power is required to pitch the wing during flapping motion. Ishihara et al [7] experimentally studied the passive pitch motion of a cranefly wing model that sunk into silicon oil. Kolomenskiy et al [8] calculated the passive pitch angle of bumblebees numerically using a torsional spring model. Their findings prove that the passive pitch motion of insects wings can be achieved using torsional spring model. Another challenge is to solve the Navier-Stokes equations for the flow field and the odorant convection-diffusion equation for the odor field with complex moving boundaries (flapping wings). Many previous researches studied the aerodynamic functions of the flapping wings using a quasi-steady model [9, 10]. This model is eligible for calculating the aerodynamics of flapping wings, but cannot be used to obtain the flow field.

In this paper, direct numerical simulations were conducted to obtain the instantaneous odor landscape. The trajectories of surging upwind and zigzagging crosswind flight were prescribed. For the flapping wings, only the leading-edge flapping motion was prescribed, while the wing pitch motion was simulated based on the aerodynamic loading using a torsional spring model. In order to mimic the odor-tracking flights, an odor source was placed in front of the fruit fly model in the upstream. All simulations were conducted using an in-house three-dimensional immersed-boundary-method-based computational fluid dynamics (CFD) solver in which the Navier-Stokes equations and the equations of motion for passive pitching wings were couple together to obtain the flow field. The odor convection-diffusion equation was then solved at each time step to resolve the odor intensity field.

## METHODOLOGY

### *Governing equations and numerical method*

The three-dimensional viscous incompressible Navier-Stokes equations are solved using an in-house immersed-boundary-method based CFD solver. The equations are written in tensor form:

$$\begin{cases} \dfrac{\partial u_i}{\partial x_i} = 0 \\ \dfrac{\partial u_i}{\partial t} + \dfrac{\partial \left(u_i u_j\right)}{\partial x_j} = -\dfrac{1}{\rho}\dfrac{\partial P}{\partial x_i} + \nu \dfrac{\partial}{\partial x_j}\left(\dfrac{\partial u_i}{\partial x_j}\right) \end{cases} \quad (1)$$

Where $u_i$ are the velocity component, $P$ is the pressure, $\rho$ is the fluid density, $\nu$ is the kinematic viscosity.

The above equations are discretized using a cell-centered, collocated arrangement of the primitive variables, and are solved using a finite difference-based immersed-boundary method [11] in a non-body-conforming Cartesian grid. The equations are integrated with time using the fractional step method. Details of the CFD solver in solving Navier–Stokes equations is elaborated and validated in our previous studies [12-14]. The CFD solver has been successfully applied to study canonical revolving wings [15-18], flapping propulsion problems [13, 19-22] and insect flight [2, 14, 23, 24].

At each time step, the Navier–Stokes equations for the fluid field and the equations of motion for solid wings are coupled and solved using an implicit method. The location and angular velocity of the wing is then updated from the previous time step. The aerodynamic forces are obtained by integrating the pressure and shear on the surface of the insect.

Once the convergence criterion is reached, the odor convection-diffusion equation is then solved based on the

velocity field to obtain the instantaneous odor intensity distribution. The odor convection-diffusion equation is written as:

$$\frac{\partial C}{\partial t}+\frac{\partial CU_i}{\partial x_i}=\alpha\frac{\partial^2 C}{\partial x_i^2} \tag{2}$$

Where $C$ is the odor intensity, $\alpha$ is the odor diffusivity, $U_i$ is the face-centered velocity obtained from interpolation of the cell-centered velocity $u_i$. The equation is then discretized using implicit method.

$$\frac{C^{n+1}-C^n}{\Delta t}+\frac{\delta C^n U_i^n}{\delta x_i}=\alpha\frac{\delta}{\delta x_i}\left(\frac{\delta C^{n+1}}{\delta x_i}\right) \tag{3}$$

Schmidt number Sc is used to indicate the intensity of odor diffusivity, which is defined as the ratio between kinematic viscosity and odor diffusivity ($\mathrm{Sc}=\nu/\alpha$). Small Sc indicates odor diffusion dominant the odor transportation, while large Sc indicates odor convection dominant the odor transportation.

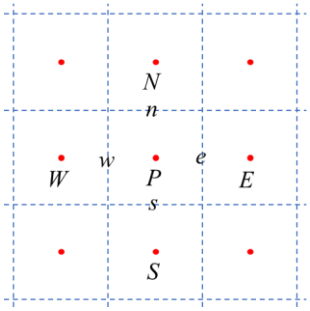


**Figure 1. Schematic of the grid. The uppercase letters denote cell-centered variables, the lowercase letters denote the face-centered variables.**

As shown in Figure 1, the Navier–Stokes equations and odor convection-diffusion equation are discretized on non-body-conforming Cartesian grid, thus eliminates the complex re-meshing algorithms for moving boundaries on body-conforming grids at each time step. The uppercase letters $W$, $E$, $N$, and $S$ represent cell-centered variables, and the lowercase letters $w$, $e$, $n$, and $s$ represent face-centered variables which are calculated by interpolation of the corresponding cell-centered variables. The differential equation for odor transportation can be written as

$$\begin{aligned}&C_P^{n+1}-\alpha\Delta t\left(a_W C_W^{n+1}+a_E C_E^{n+1}+a_N C_N^{n+1}+a_S C_S^{n+1}+a_B C_B^{n+1}+a_F C_F^{n+1}+a_P C_P^{n+1}\right)\\&=C_P^n-\Delta t\left(\frac{C_e^n U_e^n-C_w^n U_w^n}{\Delta x}+\frac{C_n^n U_n^n-C_s^n U_s^n}{\Delta y}+\frac{C_f^n U_f^n-C_b^n U_b^n}{\Delta z}\right)\end{aligned} \tag{4}$$

Where the coefficients $a_W$, $a_E$, $a_N$, $a_S$, $a_B$, $a_F$, $a_P$ are calculated by discretizing the diffusion term

$$\begin{aligned}\frac{\delta}{\delta x_i}\left(\frac{\delta C}{\delta x_i}\right)&=\frac{\frac{C_E-C_P}{\Delta x}-\frac{C_P-C_W}{\Delta x}}{\Delta x}+\frac{\frac{C_N-C_P}{\Delta y}-\frac{C_P-C_S}{\Delta y}}{\Delta y}+\frac{\frac{C_F-C_P}{\Delta z}-\frac{C_P-C_B}{\Delta z}}{\Delta z}\\&=a_E C_E+a_W C_W+a_N C_N+a_S C_S+a_F C_F+a_B C_B+a_P C_P\end{aligned} \tag{5}$$

***Wing model with torsional spring***

The fruit fly model adopted here has been used in our previous studies [2, 25]. The aspect ratio of the wing is 3.2, defined as $(\mathrm{span})^2/(\mathrm{area})$. As shown in Figure 2 (a), the kinematics of the wing is defined by three Euler angles, stroke ($\phi$), deviation ($\psi$), and pitch ($\theta$) angle. In Figure 2 (b), the stroke plane angle $\beta$ is 20°, the incline angle $\chi$ is 45°. As the wing flaps back and forth in the stroke plane with a prescribed stroke angle ($\phi$) and the wing root acting like a torsional spring, the wing pitches passively about wing leading edge.

The wing stroke angle is defined in equation (6), while the wing deviation angle is fixed as zero during the entire flapping motion. The time history of the prescribed stroke and deviation angle of the wing is shown in Figure 3.

$$\phi(t)=-A_\phi\cos(2\pi f t) \tag{6}$$

Where $\phi(t)$ is the instantaneous wing stroke angle at time $t$, $A_\phi=140°$ is the stroke amplitude, and $f$ is the flapping frequency.

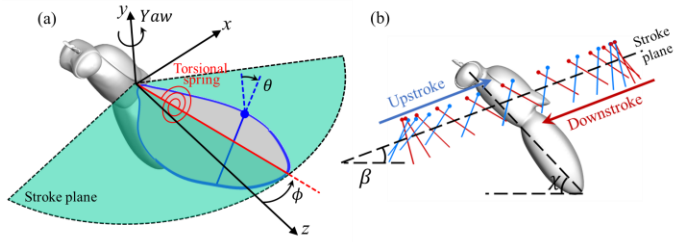


**Figure 2. Schematic of the flapping wing with a torsional spring (a) and wing chord diagram during upstroke and downstroke. Where $\theta$ is the pitch angle, $\phi$ is the stroke angle, $\beta$ is the stroke plane angle, $\chi$ is the body incline angle.**

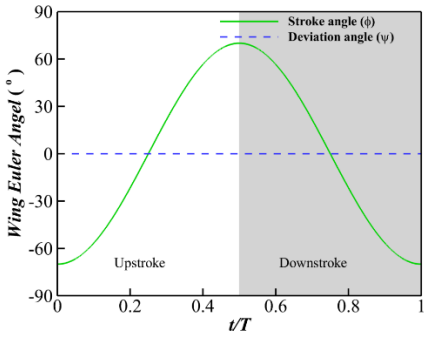


**Figure 3. The time history of prescribed stroke angle and deviation angle. In current study, the stroke amplitude $A_\phi$ is 140°, and the deviation amplitude is 0°. The gray shaded region denotes downstroke.**

By calculating the aerodynamic, elastic, and inertial forces at each time step, the passive wing pitch angle ($\theta$) is calculated using a torsional spring model, in which the wing root is represented by a torsional spring and the elastic momentum is thus obtained using

$$M_{elastic} = G(\theta - \theta_0) \tag{7}$$

Where $\theta_0$ is the rest angle, $G = 4\pi^2 f_n^2 I_{xx}$ is the torsional stiffness of the spring, $f_n$ is the natural frequency of the torsional spring, $I_{xx}$ is the moment of inertia with respect to wing leading-edge. Previous studies suggested that insects generate the necessary yaw torque in the turning maneuver by adjusting the rest angles of its bilateral wings [8, 25, 26].

The angular velocity of pitch angle is then calculated by solving the equations of motion, which can be written as follows

$$\begin{aligned} &I_{xx}\dot{\omega}_x + (I_{zz} - I_{yy})\omega_y\omega_z + I_{xy}(\omega_x\omega_z - \dot{\omega}_y) + I_{yz}(\omega_z^2 - \omega_y^2) \\ &- I_{xz}(\dot{\omega}_z + \omega_x\omega_y) = M_{aero} + M_{elastic} + M_{gravity} \end{aligned} \tag{8}$$

Where $I_{xx}$, $I_{yy}$, $I_{zz}$, $I_{xy}$, $I_{xx}$, and $I_{xz}$ are momentum of inertia of the wing. $M_{aero}$, $M_{elastic}$, and $M_{gravity}$ are the momentum due to aerodynamic, elastic, and gravitational forces, respectively.

The nondimensional torsional stiffness of the wing root is indicated by the Cauchy number Ch [7] defined as the ratio of the fluid dynamic pressure force to the structure elastic force, which can be expressed as follows:

$$Ch = \frac{\rho_{air} A_\phi^2 f^2 \bar{c}^3 b^2}{G} \tag{9}$$

Where $\bar{c}$ is the mean wing chord length, $b$ is the wing spanwise length. The Cauchy number selected in this paper is 0.15 based on our previous study [27, 28]. At which the lift coefficient is optimized.

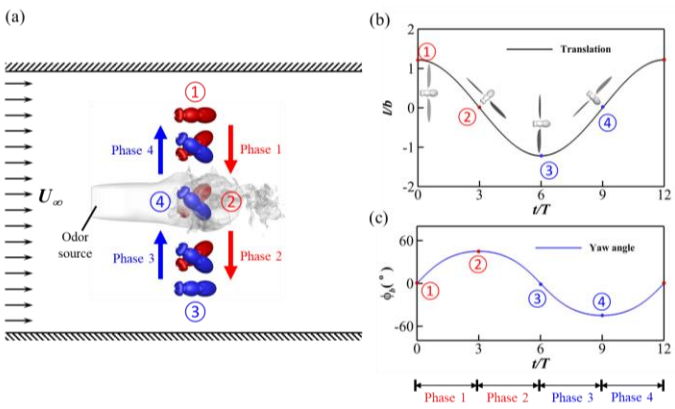


**Figure 4. Schematic diagram of the computational domain (a), time history of translation in z-direction (b) and time history of body yaw angle (c). The zigzagging motion is divided into 4 phases according to the body angular acceleration. At position ② and ④, the fruit fly zigzag through the odor plume.**

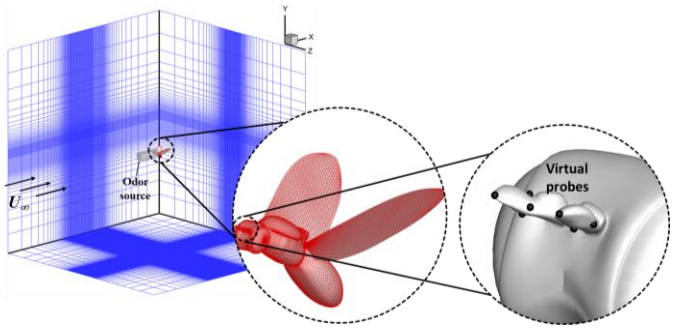


**Figure 5. Simulation setup and computational grids applied in the study. An odor source is placed in front of the fruit fly with odor intensity of 1. The antennae are represented by two virtual probes. On each of the two probes of the fruit fly, the average value of five points is used to represent the probe. The simulation is performed in a 15 million size non-uniform Cartesian grid. The body and wings are represented by high-density unstructured triangular surface mesh.**

### *Flight kinematics and simulation setup*

During a turning flight, fruit flies need to first perform a roll and yaw motion, and then a counter-roll and counter-yaw motion by subtle adjustment of the asymmetric kinematics of the left and right wings [29]. Studies have proved that the yaw torque can be achieved by adjusting the rest angle of both wings. While how the roll torque is generated requires further investigations. In this paper, the kinematics of a fruit fly was reconstructed for both surging upwind and zigzagging crosswind flight. The zigzagging motion consists of translation and pure yaw rotation in the horizontal plane, in which the roll motion is neglected.

An odor source is placed in front of the fruit fly with the odor intensity of 1. At the inlet, the odor intensity is 0. In the surging upwind case, the fruit fly is placed at a fixed location facing the odor source with the rest angle of 0. In the zigzagging crosswind flight case, the fruit fly zigzags through the odor plume. The zigzagging motion is divided into 4 phases. Figure 4 (a) shows the setup of zigzagging flight in current study. Each phase contains 3 wing flapping cycles and has different rest angle setup, as shown in Table 1. During phase 1 and 2, the fruit fly needs to generate torque that turns the body right. During phase 3 and 4, the fruit fly needs to generate torque that turns the body left.

Figure 4 (b) and (c) show the prescribed body translation in the lateral direction and rotation in the horizontal plane, respectively. The translation amplitude is 1.22$b$, and the rotation amplitude is 45°. The average relative velocity of the fruit fly body is 0.46 m/s in both cases. The inlet velocity $U_\infty$ is 0.46 m/s in surging upwind case. In order to match the same relative velocity as the surging upwind case, the inlet velocity is set as 0.39 m/s in zigzagging crosswind case.

The Reynolds number selected in this paper is 90, which is defined as $\mathrm{Re} = \bar{U}_{tip} b / \nu$, where $\bar{U}_{tip}$ is the average wingtip velocity.

**Table 1. The rest angle $\theta_0$ of left and right wings for 4 phases.**

| Phase | 1 | 2 | 3 | 4 |
|---|---|---|---|---|
| Left wing | 10° | 10° | -10° | -10° |
| Right wing | -10° | -10° | 10° | 10° |

The simulations were performed in a non-uniform Cartesian grid. The computational domain size of the simulation is $30\bar{c} \times 30\bar{c} \times 30\bar{c}$ in terms of mean wing chord length ($\bar{c}$). The grid size used in the current study is 272×112×288. As shown in Figure 5, the domain mesh has two refined layers. A high resolution in a cuboidal region around the insect is provided with the smallest resolution. Around this region, there is a secondary denser layer. Beyond the secondary denser layer, there is coarse stretched layer. Boundary conditions on all walls of the computational domain are set as Neumann boundary condition except Dirichlet boundary condition is set on the inlet wall with constant incoming velocity and odor intensity. The fruit fly body and wings are represented by high-density triangular surface mesh. The odor intensity around antennae is measured using virtual probes. Five virtual points at different locations around each antenna are selected. At each time step, the average odor intensity of the 5 points is recorded.

## RESULTS

In this section, direct numerical simulations for the two odor tracking flight motions, surging upwind and zigzagging crosswind motions were performed. The aerodynamics including passive wing pitch angle, lift coefficient, wake structure, and odor intensity will be discussed in detail. Notable differences caused by the rest angle and zigzagging motion setup were observed. In our setup, the fruit fly achieved an entire zigzagging cycle with 12 flapping cycles. We simulated the zigzagging motion for 24 flapping cycles and present the results of the last 12 flapping cycles.

Figure 6 shows the instantaneous passive wing pitch angle during both the surging upwind and zigzagging crosswind flight. The average pitch angle occurs during upstroke is -13.5° for surging upwind flight. For zigzagging crosswind flight, the number is different for each phase and wing. The average pitch angles during upstroke are -12.0°, -10.2°, -17.2°, -21.1° for the left wing and -17.2°, -21.1°, -11.5°, -10.2° for the right wing during the 4 phases, respectively. The average pitch angle occurs during downstroke is 46.3° for surging upwind flight. While for the zigzagging crosswind flight, the average pitch angles during downstroke are 49.5°, 50.2°, 40.0°, 38.7° for the left wing and 39.7°, 38.7°, 49.3°, 50.2° for the right wing during the 4 phases, respectively. Note that even though the rest angle setup is the same for phase 1 and phase 2 for zigzagging crosswind case, the pitch angle pattern and magnitude are largely different due to the asymmetic flow field. During phase 1, the fruit fly turns left and cannot capture the wake generated by the previous phase. However, during phase 2, the fruit fly is more likely to capture the wake generated previously.

The asymmetric pitch angle of the left and right wings produces asymmetric forces that generate the yaw torque. Figure 7 shows the instantaneous lift coefficient for both the surging upwind and zigzagging crosswind flight. The lift coefficient $C_L$ is defined as $C_L = \frac{2F_L}{\rho \bar{U}_{tip}^2 S}$, where $F_L$ is the lift force calculated by integrating the pressure and shear in the *y*-direction on the wing surface, *S* is the wing area. For the surging upwind case, the average lift coefficient is 1.18. The downstroke generates 82% of the total lift. For the zigzagging crosswind case, the average lift coefficient is 1.09, 1.20, 1.33, 1.21 for the left wing and 1.31, 1.21, 1.09, 1.20 for the right wing during the 4 phases, respectively. Two peaks of lift coefficient at the 3rd and 9th mid-downstroke during zigzagging crosswind flight are observed in Figure 7 (b). The possible reason is as the fruit fly turns left in phase 1, the relative velocity and angular velocity of the right wing is larger. Hence, larger lift force is generated on the right wing. This phenomenon is also observed by previous research [30] in which the effects of insect body rotation speed is investigated.

Figure 8 provides the quantitative measurement of the odor intensity on the probes during the odor tracking flight. The non-dimensional odor intensity $C^*$ is defined as $C^* = C / C_{source}$. Note that for the surging upwind case, even though the pitch angle and lift coefficient seems to reach a steady state, the odor intensity at the probe varies for different flapping cycles. As expected, the odor intensity at both probes is nearly identical for surging upwind flight. The odor intensity is maximized during downstroke and minimized during upstroke. For zigzagging crosswind flight, the odor intensity is 0 most of the time, except when the fruit fly crosses the odor plume directly. Even though the flapping wings actively draw the odor plume to the body [25], the odor plume can only be perceived during a small time interval. We saw differences in odor perception time and peak odor intensity on the two probes, as shown in Figure 8 (b). During the 3rd flapping cycle, the fruit fly crosses the odor plume from the right side to the left. The left probe intercepts the odor plume earlier than the right probe. Note that larger peak value of odor intensity is observed on the right probe. The possible reason is that the right probe is closer to the odor source. Similar phenomenon is observed during the 9th flapping cycle, when the fruit fly crosses the odor in the opposite direction. The differences in odor perception time and peak odor intensity on the left and right probes may create the stereo olfaction orientation to guide the fruit fly to the odor source during zigzagging crosswind flight.

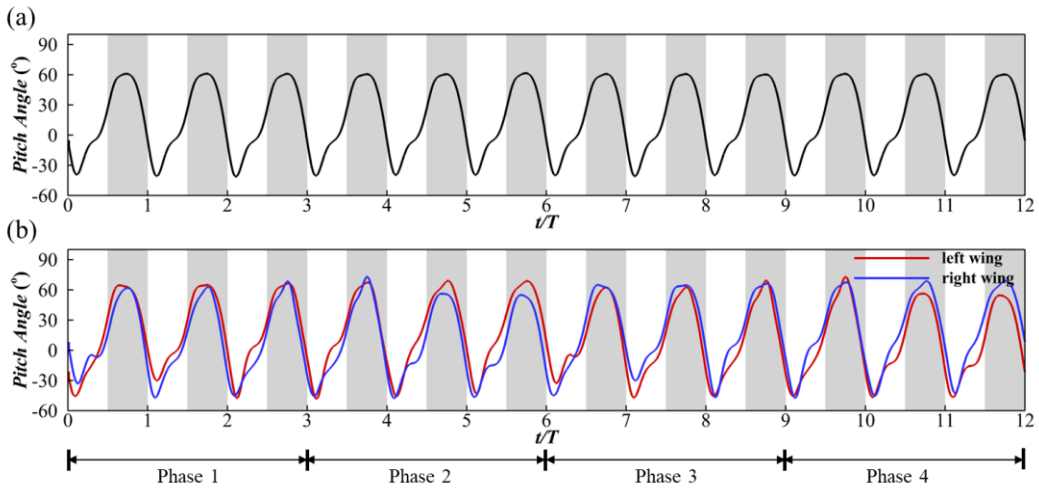


**Figure 6. Time history of the passive pitch angle of the wings in upwind surge motion (a) and zigzagging motion (b) of the fruit fly. Due to the asymmetric setup of the left and right wings in the zigzagging motion, the pitch angle of both wings is presented in (b). The gray shaded area denotes downstroke.**

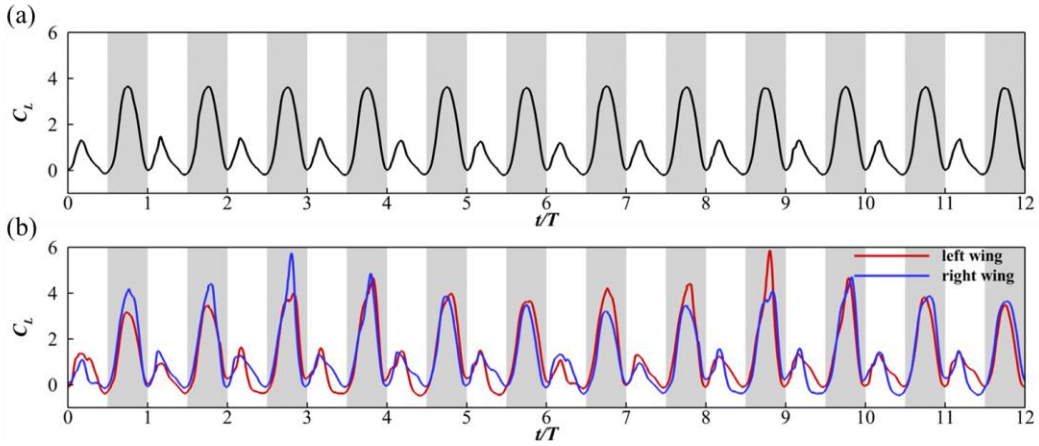


**Figure 7. Time history of the lift coefficient of the wings in upwind surge motion (a) and zigzagging motion (b) of the fruit fly. Due to the asymmetric pitch angle of the left and right wings in the zigzagging motion, the lift coefficient of both wings is presented in (b). The gray shaded area denotes downstroke.**

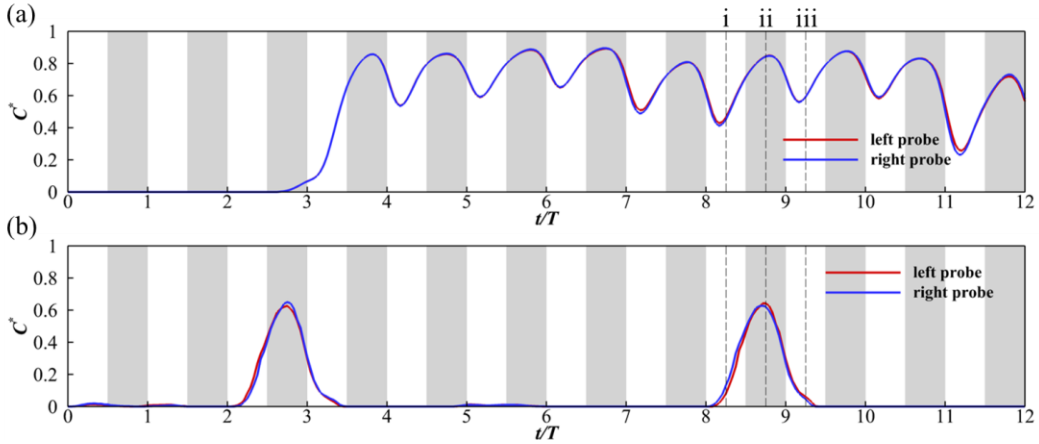


**Figure 8. Time history of the non-dimensional odor intensity at the left and right probes for upwind surge motion (a) and zigzagging motion (b) of the fruit fly. The gray shaded area denotes downstroke. Three time instants, i, ii, and iii, are selected to analyze the transient wake structure and odor plume transportation, as shown in Figure 9 and Figure 10.**

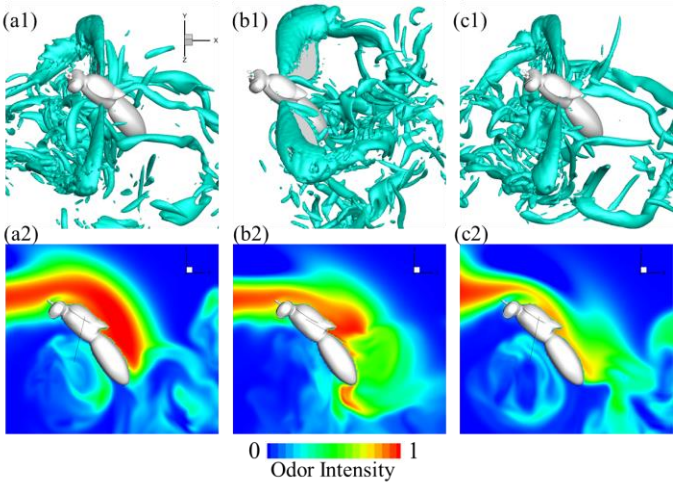


**Figure 9. Wake structure (a1), (b1), (c1), and odor contour slices (a2), (b2), (c2) generated in surging upwind flight at three instants i, ii, iii, as denoted in Figure 8. Where i and iii are the mid-upstroke, ii is the mid-downstroke. The odor contour slices are located at the body center.**

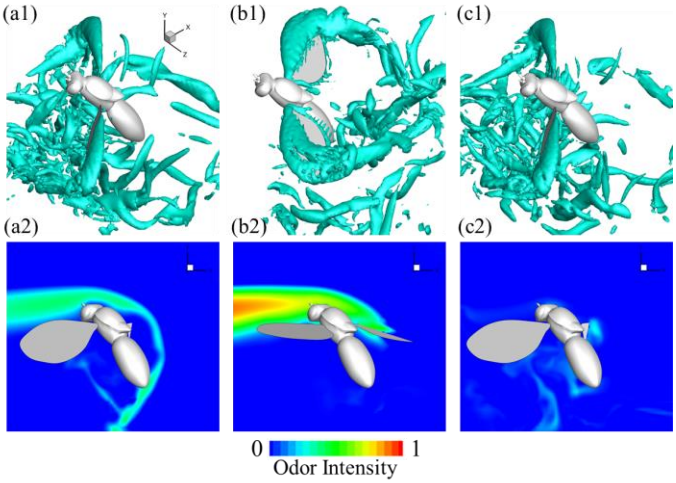


**Figure 10. Wake structure (a1), (b1), (c1), and odor contour slices (a2), (b2), (c2) generated in zigzagging flight at three instants i, ii, iii, as denoted in Figure 8. Where i and iii are the mid-upstroke, ii is the mid-downstroke. The odor contour slices are located at the middle point of the two probes.**

To illustrate the odor plume near the probes, the wake structures and odor contour slices at three different time instants for surging upwind flight is presented in Figure 9. The corresponding time instants are denoted in Figure 8. The wake structures are visualized using the iso-surface of Q-criterion. Figure 10 is the wake structures and odor contour slices during zigzagging crosswind flight. As expected, a much larger vortex is formed during the downstroke compared with the upstroke. We see from Figure 8 (a) that the odor intensity is maximized near mid-downstroke and minimized near mid-upstroke. During upstroke, the odor plume is draw upward above the probes by the wing-induced flow, as shown in Figure 9 (a2) and (c2). While during downstroke, the odor plume is draw downward to the probes by the wing-induced flow and the odor intensity is increased. This phenomenon is in line with the observation by Li et al [3] that the flapping wings trap the odor plume during downstroke and flick the odor plume during upstroke. During zigzagging crosswind flight (Figure 10), even though the odor plume is interfered by the translation motion of the insect body, it can be observed that the odor intensity is maximized at the mid-downstroke when the fruit fly cross the odor plume.

## CONCLUSIONS

The aerodynamic performance and odor intensity of surging upwind and zigzagging crosswind motions during odor tracking flight were investigated by solving the 3D Navier-Stokes equations, coupled with equations of motion for the passive pitching wings, and the convection-diffusion equation for the odor transportation. Our simulation results indicate that the odor intensity around antennae reaches its maximum value during downstroke and hits its minimum value during upstroke. In addition, the unsteady flow generated by flapping wings perturbs the odor plume structure and significantly impacts the odor intensity around the antenna. During zigzagging motion, the fruit fly can only perceive the odor plume during a small time interval. However, the differences in odor perception time and peak odor intensity between the two antennae may potentially help create the stereo olfaction orientation to guide the fruit fly for locating the odor source.

## ACKNOWLEDGMENTS

This research was supported by the National Science Foundation (CBET-2042368) and 2019 ORAU Ralph E. Powe Junior Faculty Enhancement Award to C. Li. All simulations were run on the High-Performance Computing Cluster of the College of Engineering at Villanova University.

## REFERENCES

[1] B. J. Duistermars, D. M. Chow, and M. A. Frye, "Flies require bilateral sensory input to track odor gradients in flight," *Current Biology,* vol. 19, pp. 1301-1307, 2009.

[2] C. Li, H. Dong, and K. Zhao, "A balance between aerodynamic and olfactory performance during flight in Drosophila," *Nature communications,* vol. 9, 3215, 2018.

[3] C. Li, "Effects of wing pitch kinematics on both aerodynamic and olfactory functions in an upwind surge," *Proceedings of the Institution of Mechanical Engineers, Part C: Journal of Mechanical Engineering Science,* vol. 235, pp. 296-307, 2021.

[4] F. van Breugel and M. H. Dickinson, "Plume-tracking behavior of flying Drosophila emerges from a set of

distinct sensory-motor reflexes," *Current Biology,* vol. 24, pp. 274-286, 2014.
[5] I. Balásházy, W. Hofmann, Á. Farkas, and B. G. Madas, "Three-dimensional model for aerosol transport and deposition in expanding and contracting alveoli," *Inhalation toxicology,* vol. 20, pp. 611-621, 2008.
[6] A. J. Bergou, S. Xu, and Z. J. Wang, "Passive wing pitch reversal in insect flight," *Journal of Fluid Mechanics,* vol. 591, pp. 321-337, Nov 25 2007.
[7] D. Ishihara, Y. Yamashita, T. Horie, S. Yoshida, and T. Niho, "Passive maintenance of high angle of attack and its lift generation during flapping translation in crane fly wing," *Journal of Experimental Biology,* vol. 212, pp. 3882-3891, Dec 2009.
[8] D. Kolomenskiy, S. Ravi, R. Xu, K. Ueyama, T. Jakobi, T. Engels*, et al.*, "The dynamics of passive feathering rotation in hovering flight of bumblebees," *Journal of Fluids and Structures,* vol. 91, p. 102628, 2019.
[9] J. P. Whitney and R. J. Wood, "Aeromechanics of passive rotation in flapping flight," *Journal of Fluid Mechanics,* vol. 660, pp. 197-220, 2010.
[10] Q. Wang, J. Goosen, and F. Van Keulen, "A predictive quasi-steady model of aerodynamic loads on flapping wings," *Journal of Fluid Mechanics,* vol. 800, pp. 688-719, 2016.
[11] H. Wan, H. Dong, and G. P. Huang, "Hovering hinge-connected flapping plate with passive deflection," *AIAA journal,* vol. 50, pp. 2020-2027, 2012.
[12] R. Mittal, H. Dong, M. Bozkurttas, F. Najjar, A. Vargas, and A. Von Loebbecke, "A versatile sharp interface immersed boundary method for incompressible flows with complex boundaries," *Journal of computational physics,* vol. 227, pp. 4825-4852, 2008.
[13] C. Li, H. Dong, and G. Liu, "Effects of a dynamic trailing-edge flap on the aerodynamic performance and flow structures in hovering flight," *Journal of Fluids and Structures,* vol. 58, pp. 49-65, 2015.
[14] C. Li and H. Dong, "Wing kinematics measurement and aerodynamics of a dragonfly in turning flight," *Bioinspiration & Biomimetics,* vol. 12, p. 026001, 2017.
[15] C. Li, H. Dong, and B. Cheng, "Effects of aspect ratio and angle of attack on tip vortex structures and aerodynamic performance for rotating flat plates," *AIAA 2017-3645,* p. 3645, 2017.
[16] H. Wan, H. Dong, C. Li, and Z. Liang, "Vortex Formation and Aerodynamic Force of Low Aspect-Ratio Plate in Translation and Rotation," *AIAA Paper 2012-3278,* 2012.
[17] C. Li, H. Dong, and B. Cheng, "Tip vortices formation and evolution of rotating wings at low Reynolds numbers," *Physics of Fluids,* vol. 32, p. 021905, 2020.
[18] J. Wang, C. Li, R. Zhu, G. Liu, and H. Dong, "Wake structure and aerodynamic performance of passively pitching revolving plates," *AIAA paper 2019-1376,* 2019.
[19] C. Li and H. Dong, "Three-dimensional wake topology and propulsive performance of low-aspect-ratio pitching-rolling plates," *Physics of Fluids,* vol. 28, p. 071901, 2016.
[20] J. Wang, C. Li, Y. Ren, and H. Dong, "Effects of surface morphing on the wake structure and performance of flapping plates," *AIAA paper 2017-3643,* 2017.
[21] C. Li and H. Dong, "Quantification and Analysis of Propulsive Wake Topologies in Finite Aspect-Ratio Pitching-Rolling Plates," *AIAA Paper 2016-4339,* 2016.
[22] M. Xu, M. Wei, C. Li, and H. Dong, "Adjoint-based optimization for thrust performance of three-dimensional pitching–rolling plate," *AIAA Journal,* vol. 57, pp. 3716-3727, 2019.
[23] C. Li, H. Dong, and K. Zhao, "Dual functions of insect wings in an odor-guided aeronautic navigation," *Journal of fluids engineering,* vol. 142, p. 030902, 2020.
[24] H. Dong, A. T. Bode-Oke, and C. Li, *Learning from nature: unsteady flow physics in bioinspired flapping flight*: InTech, 2018.
[25] M. Lei and C. Li, "Numerical investigation of the passive pitching mechanism in odor-tracking flights," *AIAA paper 2020-3016,* 2020.
[26] A. J. Bergou, L. Ristroph, J. Guckenheimer, I. Cohen, and Z. J. Wang, "Fruit flies modulate passive wing pitching to generate in-flight turns," *Physical review letters,* vol. 104, p. 148101, 2010.
[27] M. Lei and C. Li, "The aerodynamic performance of passive wing pitch in hovering flight," *Physics of Fluids,* vol. 32, p. 051902, 2020.
[28] C. Li, J. Wang, G. Liu, X. Deng, and H. Dong, "Passive pitching mechanism of three-dimensional flapping wings in hovering flight," in *ASME-JSME-KSME 2019 8th Joint Fluids Engineering Conference*, 2019, pp. AJKFluids2019-4639, V002T02A043.
[29] S. N. Fry, R. Sayaman, and M. H. Dickinson, "The aerodynamics of free-flight maneuvers in Drosophila," *Science,* vol. 300, pp. 495-498, 2003.
[30] S. Zeyghami, Q. Zhong, G. Liu, and H. Dong, "Passive pitching of a flapping wing in turning flight," *AIAA Journal,* vol. 57, pp. 3744-3752, 2019.